14 April 2026

Fine-tuning a machine-learned 3D cloud climatology reveals aspects of cloud cover trends

Adrià Amell[1], Simon Pfreundschuh[2], Patrick Eriksson[1]

1. Department of Environmental and Energy Sciences, Chalmers University of Technology

2. Department of Atmospheric Science, Colorado State University

Keywords

Chalmers Cloud Ice Climatology, Machine learning, Thin clouds, 3D cloud structure, Cloud cover trends, ERA5

Fine-tuning a machine-learned 3D cloud climatology reveals aspects of cloud cover trends

Adrià Amell[1], **Simon Pfreundschuh**[2], **Patrick Eriksson**[1]

[1]Department of Environmental and Energy Sciences, Chalmers University of Technology, Sweden
[2]Department of Atmospheric Science, Colorado State University, Fort Collins, USA

Corresponding author: Adrià Amell, amell@chalmers.se

Key Points:

- Fine-tuning Chalmers Cloud Ice Climatology cloud probabilities against CloudSat-CALIPSO improves the detection of previously missed clouds.
- Observational cloud cover trends with continuous spatiotemporal coverage enable multidecadal trends resolved by altitude for the first time.
- Sensitivity to thin clouds is a primary factor in reconciling inconsistent trends between satellite-based climate data records and ERA5.

Abstract

The Chalmers Cloud Ice Climatology (CCIC) is unique among long-term cloud records: using retrievals from merged geostationary 11 µm observations, it provides continuous 3D estimates of both frozen hydrometeor mass and cloud probability. Here, we present a key update to CCIC: enhanced detection of thin clouds through tuning of its neural network cloud probability outputs. The update delivers robust information from local instantaneous retrievals to long-term, large-scale averages. We compare multidecadal, height-resolved trends in cloud cover from CCIC and ERA5, revealing subtle but emerging long-term changes in total cloud cover. By exploiting CCIC's capabilities, the contributions of different cloud types and thicknesses to these changes become clearer. This helps reconcile inconsistent trends between purely observational data and ERA5, suggesting that discrepancies stem from varying sensitivities to high, thin clouds.

Plain Language Summary

Satellite observations are an essential tool to study the structure of clouds and their global distribution. However, currently available cloud-property datasets primarily provide information on the horizontal distribution of clouds. The Chalmers Cloud Ice Climatology (CCIC) overcomes this limitation by estimating several 3D cloud properties. We improved CCIC's cloud probability estimates by fine-tuning its machine-learning model with data from two reference satellites. The enhanced CCIC allows for more realistic analyses of clouds over space and time. To illustrate this, we compare CCIC with ERA5, a widely used dataset that combines observations with a numerical weather prediction model. We find that cloud trends over several decades in ERA5 differ from CCIC in a way that suggests ERA5 may unreliably estimate thin clouds, a conclusion drawn from how CCIC trends vary depending on the detection of such clouds.

1 Introduction

Information on cloud cover is essential for weather forecasting, climate studies, agrometeorology, and solar power planning. Accordingly, there is a significant number of satellite-based retrievals of cloud cover; however, none can be considered complete. Ideally, such information should have a high temporal and spatial coverage, while also providing global coverage over climate-relevant time scales. Data with high horizontal resolution exists, but it is still rare to offer a vertically-resolved cloud cover (Stubenrauch et al., 2024).

The Chalmers Cloud Ice Climatology (CCIC; Amell et al., 2024) is the first long-term cloud dataset providing high-resolution estimates of ice hydrometeor mass that are consistent with reference measurements from space-borne radar and lidar measurements. Leveraging machine-learning techniques, it enables multidecadal, quasi-global estimates of vertically resolved cloud probabilities, including cloud type, with a time resolution down to 30 min. The CCIC retrievals are based on globally gridded geostationary observations, employing only ∼11 µm radiances to provide uniform performance throughout the day, long-term stability, and data extending back to 1980.

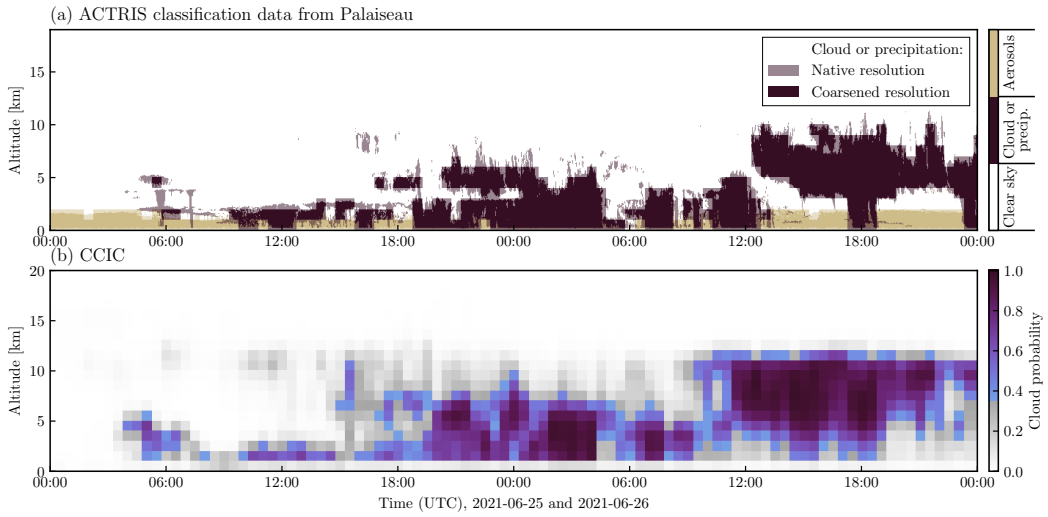

Figure 1. Comparison of instantaneous CCIC retrievals with independent retrievals. Panel (a) presents the ground-based Aerosol, Clouds and Trace Gases Research Infrastructure (ACTRIS; Laj et al., 2024) classification product at the Palaiseau site (south of Paris), and panel (b) shows the fine-tuned CCIC cloud probabilities.

CCIC has provided 3D information since its inception; fig. 1 illustrates its capability to resolve cloud probabilities at local scales (see Text S1 in the Supporting Information for details). CCIC enables direct comparisons not only with observational climate data records (CDRs), but also with reanalysis and model data. However, applications have so far focused on integrated (2D) ice hydrometeor mass data (Pfreundschuh et al., 2025; Leko, 2025; Eriksson et al., 2026). In this work, we first fine-tune the CCIC cloud probability retrievals using a more complete reference dataset than in Amell et al. (2024, hereinafter APE24). As an application, we leverage 3D retrievals to compare multidecadal trends of low, middle, high, and total cloud cover (LCC, MCC, HCC, TCC, respectively) between CCIC and ERA5 (Hersbach et al., 2020).

2 Updates to CCIC

The CCIC retrieval algorithm is a neural network trained on labelled data from CloudSat and CALIPSO retrievals. Its architecture (fig. 2 in APE24) consists of a base network that feeds into multiple independent heads, each predicting a different retrieval target: 2D cloud probability, 3D cloud type probability, and ice water path (2D) and content (3D), separately. Vertically-resolved quantities are provided on 20 equidistant levels referenced to surface elevation. CCIC supports two globally gridded geostationary inputs: NOAA CPC merged IR (CPCIR; Janowiak et al., 2001) and GridSat (Knapp et al., 2011), offering distinct advantages, detailed in Text S2.

2.1 The need for an update

In APE24, the labels used to train the ice hydrometeor mass retrievals were taken from the combined CloudSat-CALIPSO 2C-ICE product (Deng et al., 2015). In contrast, the cloud probability reference was derived from the 2B-CLDCLASS product (Sassen & Wang, 2008), which does not make use of CALIOP measurements. Without lidar information, 2B-CLDCLASS obtains reduced sensitivity to thin or multilayer clouds, lower accuracy in cloud-top retrievals and cloud type classification, and low cloud occurrence overall; specifically, less than 50 % of its profiles contain a cloud. These limitations are particularly significant for cirrus and other ice clouds that may be optically thin but play an important role in the atmosphere. Fortunately, 2B-CLDCLASS-LIDAR (Sassen et al., 2008), which combines lidar and radar measurements, provides the more complete cloud information for improved training labels; their use enables the CCIC retrieval to potentially capture clouds missed in APE24. With these improved detections, the cloudy column frequency in 2B-CLDCLASS-LIDAR exceeds 70 %, reflecting the presence of optically thin layers now included in the training set. A visual comparison between the two reference products is shown in fig. S1.

2.2 Fine-tuning

The fine-tuning of CCIC targets the limitations of its cloud probability estimates by replacing the APE24 training labels with 2B-CLDCLASS-LIDAR data. To achieve this, we first built a database of collocations following the methodology in APE24, and created analogous dataset splits (training and validation: years 2006–2009; held-out test: 2010). Then, we trained with the same process as in APE24, but with a critical distinction: all parameters outside the cloud probability heads were not updated, thus exactly preserving the retrieval output for ice hydrometeor masses.

2.3 Accuracy on test set

We evaluated the performance of the updated CCIC retrievals, extending the analysis of APE24. The Supporting Information compiles tables and figures that replicate previous results; here, we further characterize the retrievals' vertical structure. Importantly, because the APE24 test set uses a different data product with distinct statistics (e.g., reduced cloudiness), any performance shifts must be interpreted with the differing composition of the evaluation targets in mind.

2.3.1 Binary cloud masks

Given that CCIC retrieves the probability of cloud in each grid cell, we threshold this probability to answer the question "is there a cloud?", obtaining a binary mask. Pixels or voxels above the threshold are flagged as cloudy. By varying this threshold, we compute CCIC's precision and recall curves (fig. S2). We define the optimal threshold as the value minimizing the distance to the ideal precision and recall of 100 %. With this threshold, the 3D cloud mask shows a precision and recall of ∼67 % and ∼72 %, while the 2D

mask exceeds 90 % for both metrics (detailed values in table S3). Beyond these statistics, the fine-tuned model achieves greater physical consistency with the lidar-radar reference. This is qualitatively evident from the spatial patterns of the 2D and 3D masks (figs. S3 and S4), where CCIC now successfully captures thin cloud structures that APE24 fails to resolve. All subsequent results use the optimal thresholds (∼0.49 for 2D and ∼0.35 for 3D) unless stated otherwise.

2.3.2 Cloud type

Based on fig. 2, CCIC demonstrates consistency with the reference data in both zonal distribution and vertical extent, though the retrieval quality of the rarest low-level clouds (table S2) is limited. Compared to APE24, cirrus clouds show a greater vertical extent and an upward shift in their distribution. In turn, deep convection has become more geographically confined to tropical latitudes.

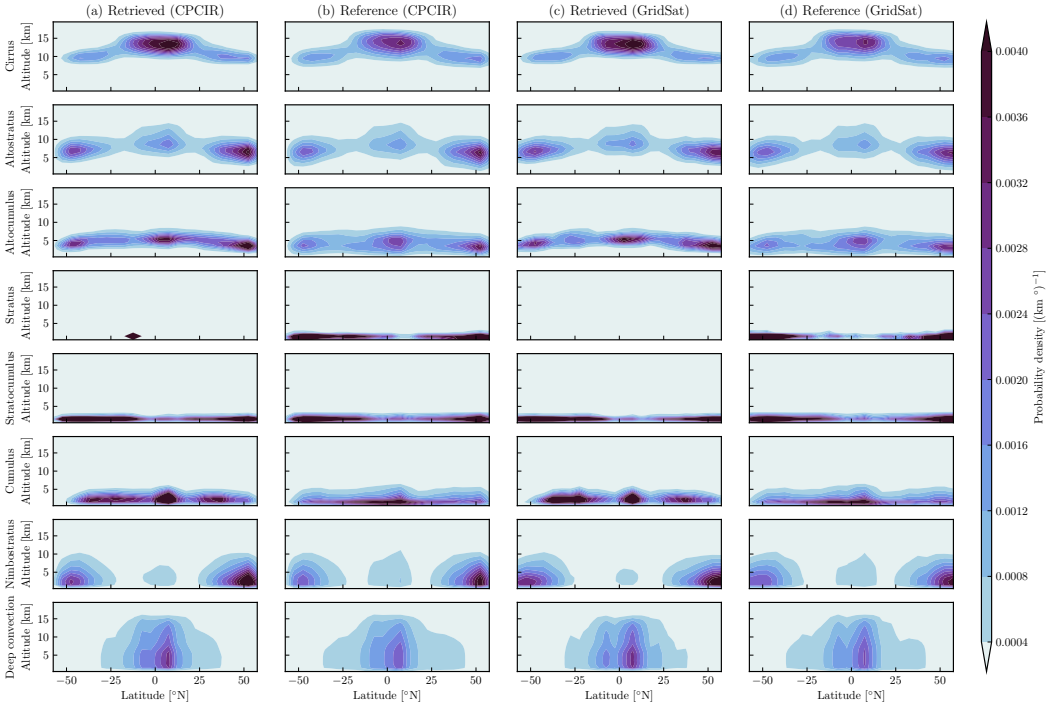

Figure 2. Spatial distribution of retrieved cloud classes and 2B-CLDCLASS-LIDAR-based reference cloud classes for the test set. Each row of panels shows the distribution of one of the eight cloud classes distinguished by the 2B-CLDCLASS-LIDAR product.

To assess classification errors, we compare predicted versus reference cloud types in a confusion matrix (fig. S5). The results indicate a strong diagonal, confirming high classification precision: detected clouds are mostly assigned the correct type. However, the matrix also reveals a tendency to underestimate cloud occurrence relative to the reference. Specifically, compared to APE24, classification performance for cirrus, altocumulus, and stratocumulus has improved, whereas cumulus and deep convection show slightly lower scores.

2.3.3 Vertical structure

Although CCIC is inherently constrained by the limited information content of the infrared observations, the previous sections demonstrate its skill in 3D cloud detection and classification. To further characterize its ability to reproduce 3D cloud structures beyond the metrics used in APE24, we provide the following statistics.

2.3.3.1 Column cloudiness. The retrieved column cloudiness (fraction of cloudy height bins) aligns closely with the reference values as shown in fig. 3, except at low cloudiness fractions. For values $\leq 10\,\%$ (at most 2 km of total column cloudiness), CCIC tends to overestimate zero cloudiness and underestimate the smallest non-zero fractions, indicating difficulty in accurately characterizing the thinnest cloud scenarios.

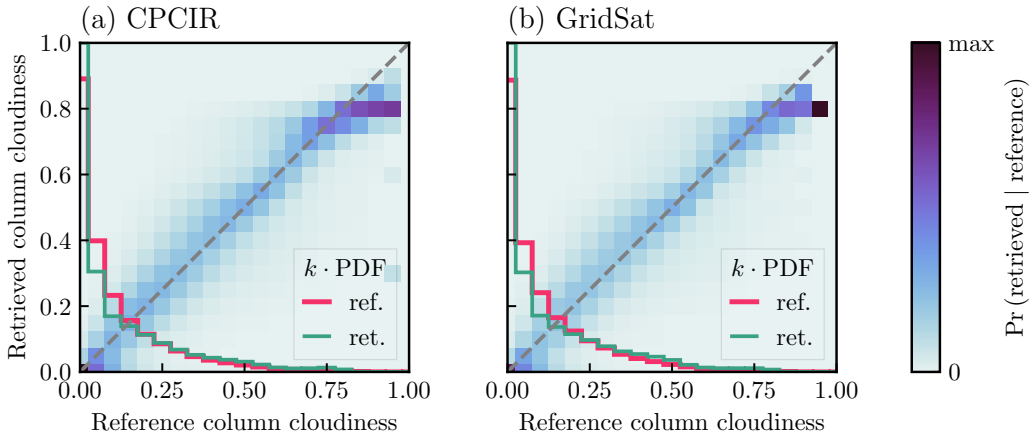

Figure 3. Retrieved column cloudiness for the test set. Column cloudiness is defined as the fraction of height bins flagged as cloudy using the thresholds from table S3. Superposed lines indicate the probability density functions (PDFs) of the retrieved and reference data, both scaled by a common constant k for each panel.

2.3.3.2 Multilayer clouds. Although the reference allows up to ten layers, fewer than 2 % of profiles in the database contain more than two. CCIC nearly always detects at most two layers (fig. S6). Despite this limitation, CCIC correctly identifies the layer count 70 % of the time when two or fewer are present.

2.3.3.3 Single-layer vertical extent. More than 30 % of the profiles show a single cloud layer in both retrieval and reference. Overall, the probability density functions of vertical extent, cloud top height, and cloud base height for these single-layer clouds are largely similar (fig. S7). The main differences are in the thinnest clouds, which occur less frequently than in the reference, and in cloud base heights, which CCIC tends to place too low. Cloud top heights are generally well estimated (with minor discrepancies near 2 km altitude). The zonal means (presented in fig. S8) support these patterns: retrieved cloud top heights agree well with the reference, while the remaining vertical structure is less consistent, yielding a global vertical extent bias of about 0.5 km. Although based on a product independent of the reference data and limited to a single location, fig. 1 helps contextualize this overestimation.

3 From cloud probabilities to cloud cover

CCIC outputs cloud probabilities reflecting the training labels: each collocation is represented by a randomly sampled 2B-CLDCLASS-LIDAR profile with a binary label (clear or cloudy) for the 2D case, and a multiclass label (clear plus eight cloud types) for the 3D case. As both cases neglect any information on the underlying subgrid cloud fraction, the retrieved probability is the likelihood that one or more clouds are present in the grid cell.

Cloud cover, in contrast, is the fraction of a grid cell covered by clouds. Following standard practice, we compute it by averaging binary cloud masks over a coarser grid. We use the ERA5 grid and implement a weighted combination of maximum and random cloud overlap assumptions for LCC, MCC, and HCC (see Text S3 for details).

The threshold t used to convert probabilities to binary masks governs the resulting cloud cover. While the optimal threshold t^* balances precision and recall, t can be tuned to match a target cloud cover using strict (large t) or lenient (small t) values. Such an adjustment shifts the ratio of false positives to false negatives, while preserving broad spatial characteristics.

The results for TCC also depend on whether the 2D cloud mask or a vertical projection of the 3D mask is employed. CCIC is trained on separate 2D and 3D masks created with different sampling strategies: the 2D mask better reflects retrievals from an active sensor as no filtering is employed, while the 3D mask tends to discard geometrically thin clouds because only a subset of vertical levels is sampled to reduce computational demands and simplify the retrieval (Text S4). As a consequence, the 2D-derived cloud cover typically exceeds the 3D-projected estimate when using the optimal thresholds, as is illustrated in fig. 4. Crucially, fig. 4 also demonstrates that differences in cloud cover due to sampling and mask construction can be partly mitigated by threshold tuning.

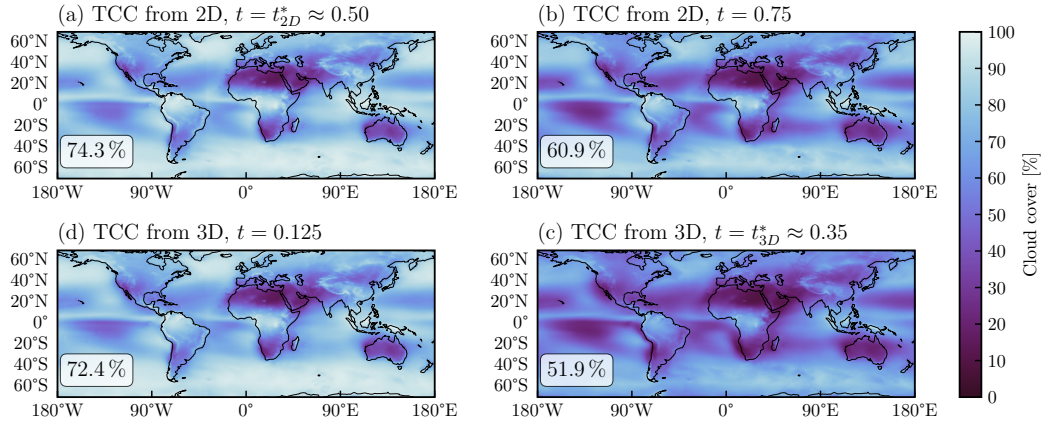

Figure 4. Average local (maps) and global (text inset) TCC from CCIC for 1991–2020. Panel titles specify the mask source (2D or 3D cloud mask) and the probability threshold.

4 Cloud cover trends

To investigate long-term trends, we execute CCIC retrievals using GridSat as input. The intersatellite homogenization of this gridded dataset provides a basis for ob-

servational consistency, despite inherent data gaps in the record. The resulting CCIC estimates are compared with ERA5 over the 70°S–70°N domain.

Figure 5 shows time series of cloud cover as differences from the current climate normal (1991–2020). Although cloud-cover variability is generally modest over four decades, several salient features emerge. Most striking is the TCC behaviour, where CCIC reveals two distinct trends depending on the detection threshold, as discussed below. ERA5 shows a strong correlation between TCC and HCC, including an abrupt increase around year 2000. Throughout the period analysed, MCC trends agree closely between the two datasets. Finally, regarding low-level clouds, a pronounced drop appears in ERA5 LCC during 2023.

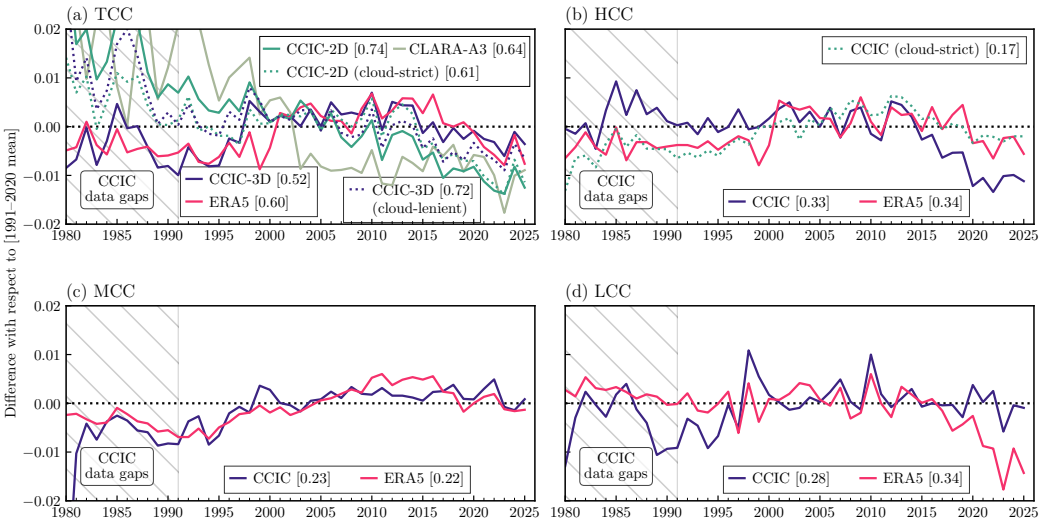

Figure 5. Yearly means of cloud cover in the CCIC domain, weighted by area. Numbers in parentheses show the climate normal mean. For CCIC, solid lines obtained with the optimal probability threshold; cloud-lenient and cloud-strict with 0.125 and 0.75 as thresholds, respectively, chosen according to Text S5. In (a), '2D' or '3D' indicates if TCC is derived from the 2D or 3D cloud mask.

CCIC shows a nearly linear decline of −0.75 % per decade since 1980 for its 2D-derived TCC. This is consistent with recent assessments of TCC from observational CDRs, which also report negative trends ranging from −0.76 % to −1.47 % per decade (Devasthale & Karlsson, 2023); we illustrate this in fig. 5a with the trend from the CLARA-A3 CDR (Karlsson, Stengel, et al., 2023), which is based on sun-synchronous satellite measurements. This decline is also observed when CCIC-2D TCC is computed using a higher confidence threshold for cloud detection, though the trend is less pronounced. The threshold also affects the absolute TCC value, as discussed in section 3: the cloud-strict threshold yields a TCC closer to CDRs from passive instruments, which report global mean values around 65 % (Karlsson, Devasthale, & Eliasson, 2023), whereas the optimal threshold TCC aligns more closely with the radar-lidar retrievals used as training labels. In contrast, both ERA5 and CCIC-3D indicate that, while TCC is declining since 2015, it remained relatively stable before 2000, below the climate normal value. For CCIC, this discontinuity is unlikely to arise solely from changes in the observational system, because it is not reflected in its 2D-derived TCC. We therefore hypothesize that the discrepancy between CCIC TCC trends is largely due to the thinnest clouds, which are expected to be underestimated in its 3D retrievals. This is further supported by the CCIC-3D cloud-lenient TCC trend, which captures thin clouds that are otherwise hard to detect and reconciles with CCIC-2D, exhibiting both a decreasing trend and a TCC exceeding 70 %,

confirming the role of thin clouds in the discrepancy (see fig. S10 for the evolution of column cloudiness by threshold).

A similar limitation in representing thin clouds may explain the ERA5 behaviour, as this reanalysis identifies clouds from relative humidity, which is inherently less sensitive to thin cloud layers. A dry bias in ERA5, evidenced by studies of aviation contrails (e.g., Wolf et al., 2025), further supports this expectation. The strong alignment between the cloud-strict CCIC-3D and ERA5 patterns in TCC suggests a shared insensitivity to changes in thin clouds. ERA5, however, lacks CCIC's ability to directly diagnose this limitation through detection thresholds. ERA5's TCC trend therefore likely captures only the contribution from optically thicker clouds and underestimates the full magnitude of climatological change.

The interpretation of a lack of sensitivity in ERA5 to changes in thin clouds is reinforced by the pronounced interannual correlation between TCC and HCC in ERA5, which suggests that ERA5 TCC is primarily driven by the variability of high clouds. The fact that this alignment appears in CCIC only under stricter confidence conditions suggests that any agreement between ERA5 and CDRs is strongest for optically thick clouds that are unambiguously detected, which is consistent with ERA5 inadequately resolving thin clouds. Our findings support the hypothesis that the declining TCC trend becomes evident only in products with adequate sensitivity to thin clouds. This underscores how retrieval sensitivity and confidence metrics can significantly influence not only the extent to which trends reflect true radiative signals but also the interpretation of climate variability and feedbacks.

The pronounced 2023 anomaly in ERA5 LCC—far exceeding the CCIC estimate—exemplifies the challenges of retrieving low-level clouds from space. CCIC struggles when high clouds obscure the scene or clouds are very low: infrared attenuation and weak brightness temperature contrast between clouds and the surface reduce the retrieval sensitivity, forcing reliance on CloudSat-CALIPSO priors. Conversely, ERA5 avoids this observational constraint but introduces model-dependent biases that may amplify LCC variability beyond physical reality (Goessling et al., 2025). The resulting LCC trend divergence contrasts sharply with the general agreement in MCC, underscoring how vertical cloud structure further complicates the retrieval and modelling challenges discussed above for thin clouds.

Both CCIC and ERA5 also enable computing trends at the local level. However, drawing clear conclusions about how trends vary spatially is hindered by several factors, of which we highlight two. First, visualizing trends requires a statistical summary, but familiar metrics like a linear rate may oversimplify complex behaviours. Second, comparing maps showing local trends between CCIC and ERA5 is inherently challenging due to the complexity of spatial patterns. Nevertheless, we provide CCIC and ERA5 local trends in the Supporting Information (fig. S11). As in our global trend analysis, CCIC-2D and ERA5 show a noticeable disagreement in TCC, with the most pronounced discrepancies—often involving opposing trends—occurring over the Atlantic, western Indian Ocean, and the southernmost latitudes. However, consistency improves considerably when comparing with CCIC-3D. Moreover, mirroring the global trends, local trends of CCIC-3D are reconciled with CCIC-2D by adjusting the probability threshold. This improvement further supports the interpretation that differing sensitivity to thin clouds likely leads to differences between ERA5 and observational data.

5 Conclusions

We upgraded the CCIC neural network presented in Amell et al. (2024) by fine-tuning with combined CloudSat and CALIPSO cloud mask training labels. As a result, CCIC is now better trained to detect thin clouds. This is not only important for more

physically complete retrievals, but also because thin clouds, particularly cirrus, contribute to a significant positive radiative feedback.

The uniqueness of the 3D CCIC retrievals, spanning multiple decades and offering quasi-global coverage, enables comparison with, e.g., ERA5. Results from different retrieval configurations within CCIC, corroborated by internal diagnostics, suggest that this reanalysis dataset fails to capture the long-term decreasing TCC trend observed in satellite climate data records, likely due to its limited ability in representing the thinnest clouds. Additional discrepancies also appear in LCC trends, where ERA5 LCC magnitudes have previously been questioned in the literature.

CCIC provides substantial benefits for clouds and climate research. Its comprehensive retrievals allow, among other things, fully resolving the diurnal cycle, discriminating between single and multilayer clouds, or tracking cloud types. They also allow conditioning on unobscured cloud levels or subsampling to match specific satellite overpasses, facilitating fair comparisons with other retrieval products. Given these capabilities, previous assessments of cloud retrieval datasets (e.g., Stubenrauch et al., 2024) can be further expanded. Similarly, CCIC may stimulate the retrieval of more 3D cloud properties from existing or upcoming globally gridded geostationary datasets (e.g., Heidinger et al., 2025).

Open Research Section

The updated CCIC is available at `https://doi.org/10.5281/zenodo.19234405` (Amell & Pfreundschuh, 2026), with the training database at `https://doi.org/10.5281/zenodo.18245282` (Amell, 2026b). The yearly means used here together with the code used to prepare and analyse them can be found at `https://doi.org/10.5281/zenodo.18246487` (Amell, 2026a); CCIC retrievals at the native resolution are not published due to the data size (10 TiB) but can be provided upon request. The following links (all last accessed on 2026-01-14) provide the source of the other datasets used in this work. The ACTRIS classification product is available from the ACTRIS Data Centre hosted by the Finnish Meteorological Institute at `https://hdl.handle.net/21.12132/1.3b2badd515e54a5d` and `https://hdl.handle.net/21.12132/1.6c3030b663ca468a` (Delanoë et al., 2023); CloudSat 2B-CLDCLASS-LIDAR R05 from the CloudSat Data Processing Center at `https://www.cloudsat.cira.colostate.edu/data-products/2b-cldclass-lidar`; NOAA Climate Prediction Center globally merged IR product version 1 (Janowiak et al., 2017) and GridSat-B1 version 2 (Knapp & NOAA CDR Program, 2014) input data at `https://doi.org//10.7289/V59P2ZKR` and `https://doi.org/10.5067/P4HZB9N27EKU`, respectively; ERA5 was obtained from `https://console.cloud.google.com/marketplace/product/bigquery-public-data/arco-era5` (Carver & Merose, 2023; Hersbach et al., 2017); and CLARA-A3 from `https://doi.org/10.5676/EUM_SAF_CM/CLARA_AVHRR/V003` (Karlsson, Riihelä, et al., 2023).

Conflict of Interest disclosure

The authors declare there are no conflicts of interest for this manuscript.

Acknowledgments

The work of AA and PE has been supported in part by the European Union's HORIZON Research and Innovation Programme under grant agreement no. 101120657, project ENFIELD (European Lighthouse to Manifest Trustworthy and Green AI).

The computations were enabled by resources provided by the National Academic Infrastructure for Supercomputing in Sweden (NAISS), partially funded by the Swedish

Research Council through grant agreement no. 2022-06725, Chalmers e-Commons at Chalmers, and Chalmers AI Research Centre.

References

Amell, A. (2026a). *Data and code supporting "fine-tuning a machine-learned 3D cloud climatology reveals aspects of cloud cover trends".* Zenodo. ([Data and code]) doi: 10.5281/zenodo.18246487

Amell, A. (2026b). *Training and evaluation database for the Chalmers cloud ice climatology update.* Zenodo. ([Dataset]) doi: 10.5281/zenodo.18245282

Amell, A., & Pfreundschuh, S. (2026). *See-geo/ccic: Update on 2B-CLDCLASS-LIDAR paper.* Zenodo. doi: 10.5281/zenodo.19234405

Amell, A., Pfreundschuh, S., & Eriksson, P. (2024). The Chalmers cloud ice climatology: Retrieval implementation and validation. *Atmospheric Measurement Techniques*, *17*(14), 4337–4368. doi: 10.5194/amt-17-4337-2024

Carver, R. W., & Merose, A. (2023). ARCO-ERA5: An analysis-ready cloud-optimized reanalysis dataset. In *22nd conf. on AI for env. science.* Retrieved from `https://ams.confex.com/ams/103ANNUAL/meetingapp.cgi/Paper/415842` (`https://github.com/google-research/arco-era5`, accessed on 2026-01-14)

Delanoë, J., Dupont, J.-C., Kotthaus, S., & O'Connor, E. (2023). *Classification data from Palaiseau on 25 and 26 june 2021.* ACTRIS Cloud remote sensing data centre unit (CLU). ([Dataset], `https://hdl.handle.net/21.12132/1.3b2badd515e54a5d` and `https://hdl.handle.net/21.12132/1.6c3030b663ca468a`, accessed on 2026-01-14.)

Deng, M., Mace, G. G., Wang, Z., & Berry, E. (2015). Cloudsat 2C-ICE product update with a new ze parameterization in lidar-only region. *Journal of Geophysical Research: Atmospheres*, *120*(23), 12,198-12,208. doi: https://doi.org/10.1002/2015JD023600

Devasthale, A., & Karlsson, K.-G. (2023). Decadal stability and trends in the global cloud amount and cloud top temperature in the satellite-based climate data records. *Remote Sensing*, *15*(3819). doi: 10.3390/rs15153819

Eriksson, P., Baró Pérez, A., Müller, N., Hallborn, H., May, E., Brath, M., ... Ickes, L. (2026). Advancements and continued challenges in observations and global modelling of atmospheric ice mass. *Atmospheric Chemistry and Physics*, *26*(4), 2741–2768. Retrieved from `https://acp.copernicus.org/articles/26/2741/2026/` doi: 10.5194/acp-26-2741-2026

Goessling, H. F., Rackow, T., & Jung, T. (2025). Recent global temperature surge intensified by record-low planetary albedo. *Science*, *387*(6729), 68-73. Retrieved from `https://www.science.org/doi/abs/10.1126/science.adq7280` doi: 10.1126/science.adq7280

Heidinger, A., Stephens, G., Schulz, J., John, V. O., Meirink, J. F., Stengel, M., ... Horn, C. (2025). A geo-ring of spectral radiances: toward a next generation of the international satellite cloud climatology project (ISCCP-NG). *Bulletin of the American Meteorological Society*, BAMS-D-24-0161.1. Retrieved from `https://journals.ametsoc.org/view/journals/bams/aop/BAMS-D-24-0161.1/BAMS-D-24-0161.1.xml` doi: 10.1175/BAMS-D-24-0161.1

Hersbach, H., Bell, B., Berrisford, P., Hirahara, S., Horányi, A., Muñoz-Sabater, J., ... Thépaut, J.-N. (2020). The ERA5 global reanalysis. *Quarterly Journal of the Royal Meteorological Society*, *146*(730), 1999-2049. Retrieved from `https://rmets.onlinelibrary.wiley.com/doi/abs/10.1002/qj.3803` doi: https://doi.org/10.1002/qj.3803

Hersbach, H., Bell, B., Berrisford, P., Hirahara, S., Horányi, A., Muñoz-Sabater, J., ... Thépaut, J.-N. (2017). *Complete ERA5: Fifth generation of ECMWF atmospheric reanalyses of the global climate.* Copernicus Climate Change Service

(C3S) Data Store (CDS).

Janowiak, J. E., Joyce, B., & Xie, P. (2017). *NCEP/CPC L3 half hourly 4km global (60S–60N) merged IR v1.* Greenbelt, MD: Goddard Earth Sciences Data and Information Services Center (GES DISC). (Accessed: 4 December 2025) doi: 10.5067/P4HZB9N27EKU

Janowiak, J. E., Joyce, R. J., & Yarosh, Y. (2001). A real-time global half-hourly pixel-resolution infrared dataset and its applications. *Bulletin of the American Meteorological Society*, *82*(2), 205 - 218. doi: 10.1175/1520-0477(2001)082⟨0205:ARTGHH⟩2.3.CO;2

Karlsson, K.-G., Devasthale, A., & Eliasson, S. (2023). Global cloudiness and cloud top information from AVHRR in the 42-year CLARA-A3 climate data record covering the period 1979–2020. *Remote Sensing*, *15*(3044). doi: 10.3390/rs15123044

Karlsson, K.-G., Riihelä, A., Trentmann, J., Stengel, M., Solodovnik, I., Meirink, J. F., ... Hollmann, R. (2023). *Clara-a3: Cm saf cloud, albedo and surface radiation dataset from avhrr data - edition 3.* Satellite Application Facility on Climate Monitoring (CM SAF). Retrieved from `https://wui.cmsaf.eu/safira/action/viewDoiDetails?acronym=CLARA_AVHRR_V003` doi: 10.5676/EUM_SAF_CM/CLARA_AVHRR/V003

Karlsson, K.-G., Stengel, M., Meirink, J. F., Riihelä, A., Trentmann, J., Akkermans, T., ... Hollmann, R. (2023). CLARA-A3: The third edition of the AVHRR-based CM SAF climate data record on clouds, radiation and surface albedo covering the period 1979 to 2023. *Earth System Science Data*, *15*(11), 4901–4926. Retrieved from `https://essd.copernicus.org/articles/15/4901/2023/` doi: 10.5194/essd-15-4901-2023

Knapp, K. R., Ansari, S., Bain, C. L., Bourassa, M. A., Dickinson, M. J., Funk, C., ... Magnusdottir, G. (2011). Globally Gridded Satellite Observations for Climate Studies. *Bulletin of the American Meteorological Society*, *92*(7), 893–907. doi: 10.1175/2011BAMS3039.1

Knapp, K. R., & NOAA CDR Program. (2014). *NOAA climate data record (CDR) of gridded satellite data from ISCCP B1 (GridSat-B1) infrared channel brightness temperature, version 2.* NOAA National Centers for Environmental Information. doi: 10.7289/V59P2ZKR

Laj, P., Myhre, C. L., Riffault, V., Amiridis, V., Fuchs, H., Eleftheriadis, K., ... Vana, M. (2024). Aerosol, clouds and trace gases research infrastructure (actris): The European research infrastructure supporting atmospheric science. *Bulletin of the American Meteorological Society*, *105*(7), E1098 - E1136. Retrieved from `https://journals.ametsoc.org/view/journals/bams/105/7/BAMS-D-23-0064.1.xml` doi: 10.1175/BAMS-D-23-0064.1

Leko, L. (2025). *The diurnal cycle of cloud ice water path.*

Pfreundschuh, S., Kukulies, J., Amell, A., Hallborn, H., May, E., & Eriksson, P. (2025). The Chalmers cloud ice climatology: A novel robust climate record of frozen cloud hydrometeor concentrations. *Journal of Geophysical Research: Atmospheres*, *130*(6). doi: 10.1029/2024JD042618

Sassen, K., & Wang, Z. (2008). Classifying clouds around the globe with the CloudSat radar: 1-year of results. *Geophysical Research Letters*, *35*(4). doi: https://doi.org/10.1029/2007GL032591

Sassen, K., Wang, Z., & Liu, D. (2008). Global distribution of cirrus clouds from CloudSat/cloud-aerosol lidar and infrared pathfinder satellite observations (CALIPSO) measurements. *Journal of Geophysical Research: Atmospheres*, *113*(D8). doi: https://doi.org/10.1029/2008JD009972

Stubenrauch, C. J., Kinne, S., Mandorli, G., Rossow, W. B., Winker, D. M., Ackerman, S. A., ... Zhao, G. (2024, December). Lessons Learned from the Updated GEWEX Cloud Assessment Database. *Surveys in Geophysics*, *45*(6), 1999–2048. doi: 10.1007/s10712-024-09824-0

Wolf, K., Bellouin, N., Boucher, O., Rohs, S., & Li, Y. (2025). Correction of ERA5 temperature and relative humidity biases by bivariate quantile mapping for contrail formation analysis. *Atmospheric Chemistry and Physics*, *25*(1), 157–181. Retrieved from `https://acp.copernicus.org/articles/25/157/2025/` doi: 10.5194/acp-25-157-2025